Fabrication of ternary GO/g-C₃N₄/MoS₂ flower-like heterojunctions with enhanced photocatalytic activity for water remediation

Ming-hong Wu[a], Lin Li[a], Yuan-cheng Xue[a], Gang Xu[b], Liang Tang[a,*], Ning Liu[b], Wen-yuan Huang[b]

[a] School of Environmental and Chemical Engineering, Shanghai University, Shanghai 200444, PR China
[b] School of Environment and Architecture, University of Shanghai for Science and Technology, Shanghai 200093, PR China

ARTICLE INFO

ABSTRACT

It is extremely important to design excellent nanojunction to improve photocatalytic performance. In this study, we use a simple method to construct GO/g-C₃N₄/MoS₂ ternary-layered nanostructures as an effective photocatalyst for environmental purification using solar energy. The as-prepared materials have more adsorption sites and response sites due to the dual effects of NMP and CTAB. With the visible light irradiation, it has great photodegradation performance for MB, RhB and CV, as well as the photocatalytic reduction ability to Cr (VI). Meanwhile, the nanocomposites exhibit good reproducibility and stability during the cycle of the experiment. The designed heterostructures have a flower structure, which effectively improves the collection of electrons in MoS₂ and holes in g-C₃N₄, effectively reducing the binding of photogenerated electron carriers. Furthermore, GO acts as a fast transport holes, which is attributed to superior its electrical conductivity. This work provides a new field of view for establishing high-efficient and easy-made photocatalysts with environmental remediation.

1. Introduction

With the rapid development of modern industrialization and population, energy crisis and environmental pollution has become an increasingly serious problem in the world. Since the last century, industrial development and environmental protection have always been contradictory [1]. But today, with the continuous improvement of environmental awareness, people attach importance to the development and utilization of clean energy, especially the endless solar energy to deal with environmental problems [2,3]. Therefore, the development of novel functional materials has become more urgent for achieving the conversion of solar energy into chemical energy. Nanomaterials with semiconductor properties, including metal-organic frames (MOFs) [4], metal oxides [5,6], semiconductor-carbon photocatalysts [7], non-metallic materials [8] and metal sulfides [9] etc., exhibit excellent light absorption properties and environmental purification functions. Among them, the transition metal sulfides is an outstanding representative of metal sulfides, especially the layered structure of molybdenum disulfide (MoS₂) [10].

MoS₂ is a two-dimensional layered nanomaterial, whose structure consists of a three-dimensional stacked atomic layer (S−Mo−S) [11]. The overlapping layers and layers are held together by the weak van der Waals forces [12]. In addition, MoS₂ has an adjustable bandgap structure, which has direct (indirect) band-gap of 1.90 eV (1.20 eV) [13,14].

As a result, MoS₂ has been considered the most promising candidate to noble metal photocatalysts. To date, its shadow often appears in energy conversion and environmental remediation, such as batteries [7], hydrogen production [15], photocatalytic reduction of heavy metal ions [16] and photodegradation [17,18]. However, bulk MoS₂ exposes to very few active edge sites for photocatalytic reactions. Therefore, exposure to the rich active edge sites of the MoS₂ nanostructured material is urgent for the field of photocatalysis. Due to MoS₂ own anisotropy and distinctive crystal structure, MoS₂ photocatalyst can be tuned via reducing layer stacking number and expanding interlayer spacing, which can expose more active edge sites [19]. By means of special characterization, we can see that the extremely dispersed MoS₂ samples synthesized with the addition of surfactant-assisted and soft hydrothermal routes show few layers and short stripes [20–22]. Therefore, an efficient synthesis method is able to control the number of MoS₂ edge active sites in order to achieve efficient photocatalytic performance.

To achieve MoS₂ maximized photocatalytic activity, effective substrates are essential for the nucleation of MoS₂ and subsequent growth [23]. Two other 2D nanomaterials, graphene oxide (GO) and graphitic carbon nitride (g-C₃N₄, CN) are recognized as excellent catalytic substrates [24,25]. Some MoS₂/GO and MoS₂/g-C₃N₄ nanocomposites have been prepared and verified with high photocatalytic activity [26–28]. In order to solve the problem of dye wastewater and heavy metal ions pollution, photocatalyst technology is one of the most

---

economical technologies. Herein, we used GO/g-C$_3$N$_4$ hybrid as the substrate for MoS$_2$ attachment and growth. The composite base layered nanomaterials provide favorable transmission channel for photo-excited electrons [29,30]. More importantly, we prepared highly dispersed MoS$_2$ with controlled exposure to more the catalytic active edge sites by surfactant-assisted solvothermal method. Owing to the increase of photocatalytic response sites, the optical absorption ability of the prepared nanocomposites was greatly improved. To test the possibility of remediation of contaminated water, in the study, the photocatalytic oxidation processes aiming at three dyes, including methylene blue (MB), rhodamine B (RhB) and crystal violet (CV) were conducted. In the meantime, the photocatalytic elimination of toxic heavy metal Cr (VI) was also carried out by the hybrids.

2. Experimental

2.1. Synthesis of the GO and g-C$_3$N$_4$

GO was prepared from natural graphite powder by the modified Hummers method as reported in other literature [31]. The CN samples were synthesized as follows: firstly, 1 g thiourea and 4 g melamine were ground into powder and homogeneously mixed together. The mixed powder was transferred into a crucible, which was heated at 550 °C for 4 h. After cooling to room temperature, the obtained yellow CN was ground into powder. Then, 3 g CN powder was mixed with sodium hydroxide (NaOH) solution (60 mL, 3 M). The mixture was stirred at 80 °C for 2 h, followed by ultrasonication for 2 h and repeated 4 times. Then, the prepared product was centrifuged to neutral. Finally, the product was dispersed in deionized water to obtain 8 mg mL^{-1} of CN suspension.

2.2. Preparation of GO/g-C$_3$N$_4$/MoS$_2$ hybrid

An amount of 10 mL of GO (5 mg mL^{-1}) aqueous solution and 1.5 mL CN suspension were added to 20 mL of 1-methyl-2-pyrrolidi-none (NMP), and then the mixed solution was treated by sonication for 2 h to obtain brown solution. After that, 2 mL of acetic acid (CH$_3$COOH) was added to the brown solution, followed by stirring for 5 min. Then, an appropriate amount of cetyltrimethylammonium bromide (CTAB, mass of 0 g, 0.07 g, 0.15 g, 0.22 g) was dissolved in 10 mL of deionized water, which was slowly added to the mixture solution. After 12 h of stirring, 0.45 g of sodium molybdate (Na$_2$MoO$_4$) and 0.57 g thiourea were added into the mixture solution, which was stirred quickly for 1h. The resulting suspension was transferred into a Teflon-lined stainless steel autoclave, which was heated at 200 °C for 24 h. After natural cooling, the dark product was centrifuged and washed three times with ethanol and deionized water. Eventually, the product was freeze-dried for 24 h. The final product was named GCM-0, GCM-7, GCM-15, GCM-22, respectively. A schematic diagram of the preparation procedure is briefly shown in Scheme Scheme 1.

In order to explore the effect of CH$_3$COOH and NMP on the composites, the synthesized nanocomposites were named GCM-15-NAA when the amount of immobilized CTAB was 0.15 g and the CH$_3$COOH was absent. Another sample changed only 20 mL deionized water instead of NMP, and the synthetic composite material was labeled as GCM-15-DI. For comparison, the pure MoS$_2$ was synthesized via the same method without others.

### 2.3. Characterization of GO/g-C$_3$N$_4$/MoS$_2$ hybrid

The transmission electron microscope (TEM) images were examined on a FEI Tecnai G2 F20 microscope at the accelerating voltage of 200 kV. The powder X-ray diffraction (XRD) patterns were performed on a Bruker D8 Advance using Cu Kα radiation operated at 40 kV and 40 mA. Scanning electronic microscopy (SEM) images were taken with Hitachi FESEM-4800. Fourier transform infrared spectroscopy (FT-IR) was obtained with Thermo Nicolet Avatar 370 FT-IR. UV–vis diffuse reflectance spectra (DRS) were carried out at room temperature on Agilent Cary 100 spectrometer. X-Ray photoelectron spectrometer (XPS) surveys were documented using a Kratos Axis Ultra DLD X-ray photoelectron spectrometer. The Brunauer–Emmett–Teller surface (BET) areas and pore size distributions were collected by N$_2$ adsorption (Quan-tachrome autosorb-iQ-2MP). The photoluminescence (PL) spectra were recorded on a Hitachi F-7000 fluorescence spectro-photometer at an excitation wavelength of 360 nm.

2.4. Evaluation of photocatalytic activity

The photocatalytic performance of the as-prepared samples was assessed by the degradation of methyl blue (MB, 20 mg L^{-1}) under 300 W Xe lamp (Nanjing Sidongke Electrical Equipment Co., China) with a cut off filter (λ > 420 nm). 20 mg photocatalyst was placed in a 50 mL MB solution in a 60 mL quartz tube. In general, in order to achieve adsorption-desorption equilibrium, the dye solution was stirred for 30 min in the dark. According to the pre-set time interval, 1.0 mL solution was taken out and analyzed with a UV–vis spectrophotometer at the maximal absorption wavelength of MB (664 nm). Similarly, the photodegradation for rhodamine B (RhB, 20 mg L^{-1}), crystal violet (CV, 20 mg L^{-1}) and photoreduction for Cr (VI) (10 mg L^{-1}) were tested under the visible-light illumination. In particular, the concentration of Cr (VI) was determined by means of diphenylcarbazide method (DPC) with a UV–vis spectrophotometer.

2.5. Photoelectrochemical measurements

The photocurrent measurements, Mott-Schottky analysis and electrochemical impedance spectroscopy (EIS) were conducted on an electrochemical workstation (CHI660E Instruments). The photoelectrode was prepared according to the method described by Zhao et al. [32]. The conventional three-electrode uses the catalyst composite as a working electrode, a Pt foil as a counter electrode and a saturated calomel electrode (SCE) as a reference electrode. Amperometric I–t curves
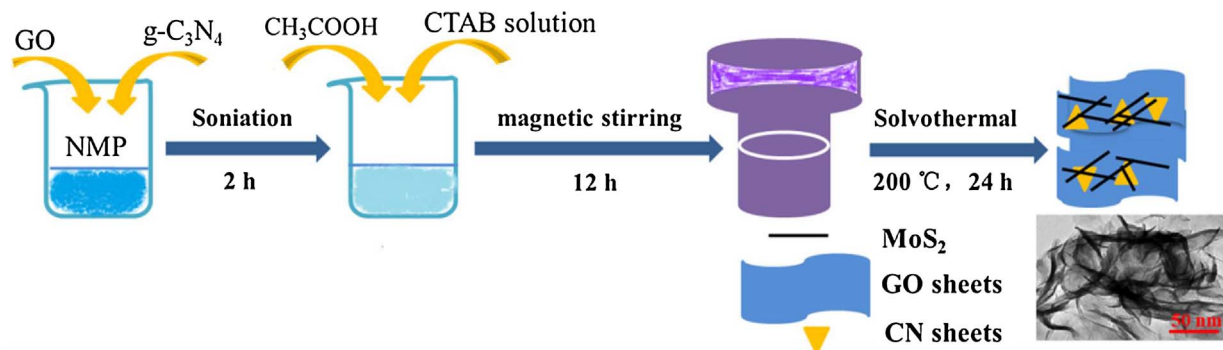
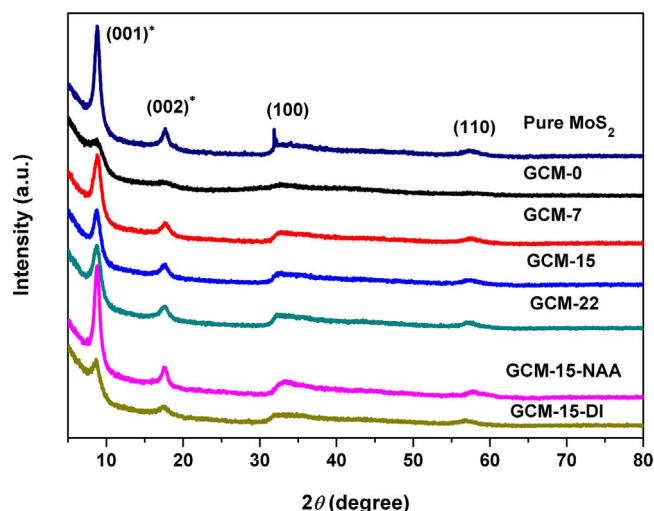**Scheme 1.** Schematic diagram of the preparation procedure for the hybrid.

Fig. 1. XRD patterns of pure MoS$_2$ and GCM nanocomposites.

Fig. 2. FT-IR spectra of pure MoS$_2$ and GCM samples.

were determined at a 0.5 V bias voltage potential (vs SCE). A 500 W Xe arc lamp with a 420 nm cutoff was used as the light source. The Mott-Schottky measurements were taken with impedance-potential model measure the band positions of the g-C$_3$N$_4$ and MoS$_2$. EIS tests were carried out in the dark circumstance at open circuit potential over the frequency range between 10^5 and 10^{-2} Hz. All of the experiments were performed in 0.5 M Na$_2$SO$_4$ solution under the room temperature.

3. Results and discussion

3.1. Fabrication and characterization

Fig. 1 shows the XRD patterns of pure MoS$_2$ and GCM composite samples. The diffraction peaks of pure MoS$_2$ are completely consistent with the previously reported MoS$_2$ [33,34], indicating that these photocatalysts have been successfully synthesized. For the pure MoS$_2$, the characteristic diffraction peaks located at 32.7° and 58.3° unambiguously can be assigned to the (100) and (110) planes of 2H–MoS$_2$ [35]. However, It is noteworthy that the typical (002) reflection peak located at 14.3° is divided into two different diffraction peaks located at 9.3° and 17.7° (labeled as (001)* and (002)*, respectively), which is attributed to the expansion of the layer spacing [36,37]. The change in layer spacing may be due to the combined effect of CTAB and NMP. The evolution of the layered structure from the dense state to the expansion causes MoS$_2$ to obtain more photocatalytic reactive sites, which is beneficial to the photocatalytic ability of the composites. Meanwhile, as can be seen from the Fig. S1, the intensity of (100) and (002) peaks obviously decreased after hydrolysis. It is shown that hydrolysis made the layered g-C$_3$N$_4$ thinner and reduced the order between the interplanar [38]. The result indicated that the original CN was successfully hydrolyzed. FT-IR spectra of the MoS$_2$ and GO/g-C$_3$N$_4$/ MoS$_2$ composites are shown Fig. 2. For MoS$_2$, we observe the peaks at 524 and 956 cm^{-1} due to Mo−S and Mo−O stretching vibrations. Owing to S═O asymmetric stretching vibration, the absorption peak is observed at 1120 cm^{-1} [39]. As expected, the same characteristic peaks are observed for the synthetic nanomaterials. The characteristic FT-IR spectrum (Fig. S2) of the GCM-7 is not clearly observed stretching vibration modes at 1250–1700 cm^{-1} and tri-s-triazine ring units at around 800 cm^{-1}, which is due to the low content of g-C$_3$N$_4$ in the composite.

The surface morphology and structure of as-prepared composite is observed by SEM and TEM images as shown in Fig. 3. It is clearly illustrated in Fig. 3a that GCM-7 nanocomposite presents three-dimensional flower like structure, which is in accord with the previous observations of MoS$_2$ [40]. As illustrated in Fig. 3b–c, MoS$_2$ nanosheets are in close contact with the GO/g-C$_3$N$_4$ substrate, which provides a
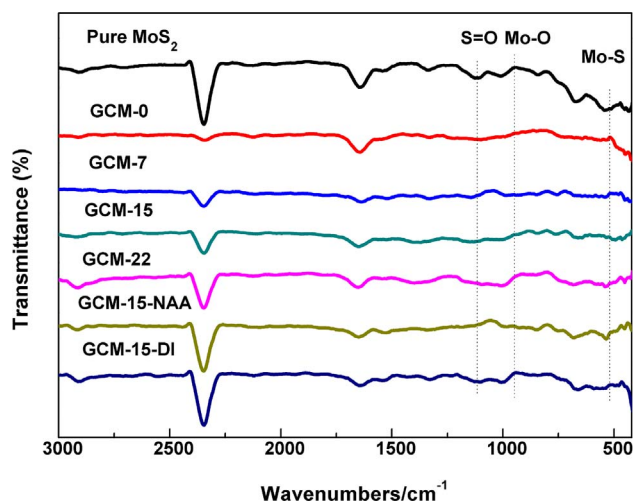
path for the conduction of photogenerated electrons. Meanwhile, MoS$_2$ nanosheets are highly dispersed in the GCM hybrids, which can greatly enhance the transmission of photo-generated electrons. Fig. 3d shows that the lattice distance of MoS$_2$ is measured as 0.213 nm. It is clear that the MoS$_2$ lamellar structure is embedded in the GO/g-C$_3$N$_4$ substrate, indicating that MoS$_2$ has successfully constructed complex heterojunctions. Based on the analysis of SEM and TEM, it can be proved that MoS$_2$ flakes can be successfully embedded into the surface of GO/g-C$_3$N$_4$ by mild solvothermal method to form composite heterojunction structure and enhance the transfer efficiency of photogenerated electrons. The composition analysis is performed by energy-dispersive X-ray spectroscopy (EDS) measurement, indicating that there are C, N, O, S and Mo elements in the GCM-7 hybrids. In addition, the EDS element mapping (Fig. S3) and spectrum (Fig. S4) show that these elements are evenly distributed throughout the GCM-7.

In order to explore the porous properties of the as-prepared samples, the BET surface area and pore size distribution of the samples are performed via nitrogen adsorption–desorption isotherms method. The BET surface area, pore size distributions and the full data are shown in Table 1. It can be seen that the BET surface area of GCM-7 nanocomposites is 97.562 m^2 g^{-1}, which is higher than others. One possibility is that MoS$_2$ is doubly influenced by both acetic acid and CTAB during growth. Another possible explanation is that the solvent has a significant effect on the spatial structure of MoS$_2$. It also confirms that GCM-7 can provide more adsorption and photocatalytic active sites. According to the IUPAC classification [41], the adsorption-desorption isotherms are IV isotherms with H3 typical hysteresis loops, as shown in Fig. 4. At the high relative pressure (P/P$_0$), the GCM-7 nanomaterial presents high adsorption properties, elucidating the existence of cumulative holes [42,43]. The pore size distributions are confirmed using desorption data by the Barrett-Joyner-Halenda (BJH) method, which is inserted in Fig. 4. The pore size distribution curve shows that the hybrid displays a relatively narrow distribution in the range of 1–6 nm, which may be attributed to the dual effect of surfactant and solvent to make MoS$_2$ highly dispersed.

X-ray photoelectron spectroscopy (XPS) is used to further study the chemical bonding state and elemental composition of GCM-7 (Fig. 5). The overall XPS survey spectrum (Fig. 5a) suggests C, N, Mo, S and O elements as the main elemental components present in GCM-7 hybrid. In Fig. 5b, the high-resolution XPS spectra of O 1s have been listed. The two peaks at 530.4 and 532.3 eV can be matched with the oxygen components of the GO and the carbonyl group in acetic acid. Fig. 5c shows the deconvolution of the sample XPS C 1s spectrum. There are three binding energy peaks at 283.7, 284.8 and 285.3 eV. The peaks at 283.7 and 285.3 eV are corresponding to C−C bond and C−N bond
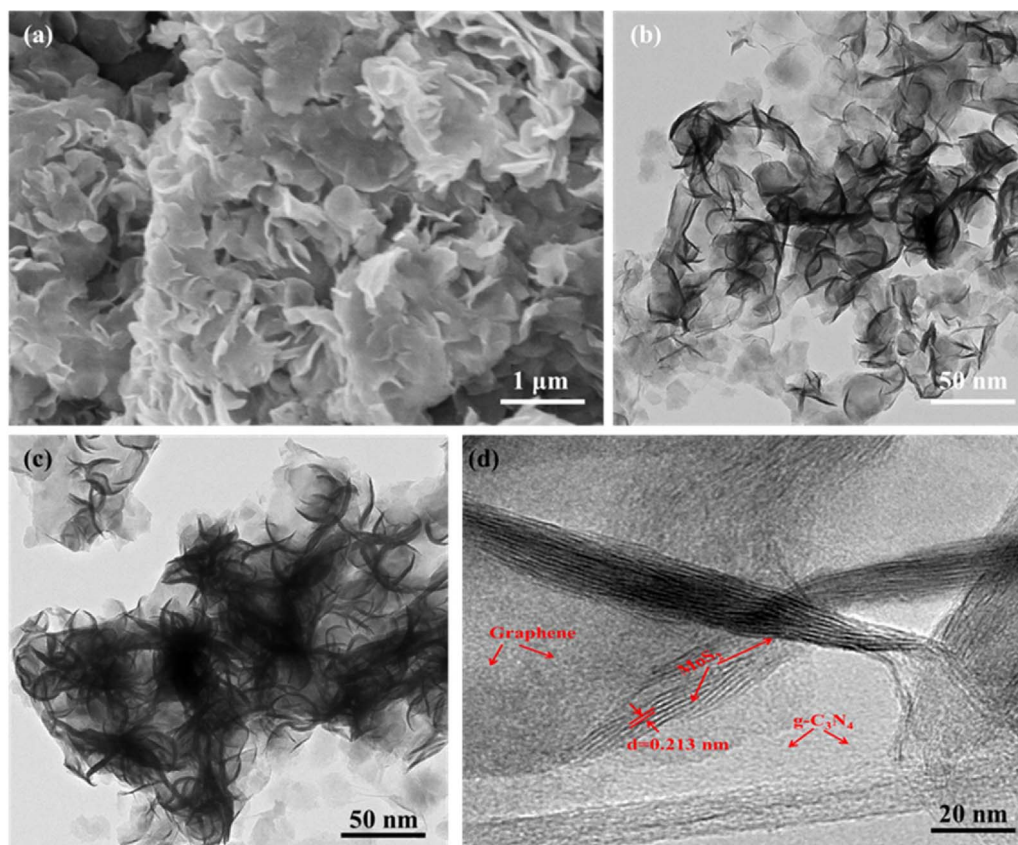
Table 1
BET specific surface area, pore volume and pore diameter of as-prepared samples.

Samples	BET(m^2/g)[a]	Pore Volume (cc/g)[b]	Pore Diameter (nm)[c]
GCM-0	92.415	0.535	4. 319
GCM-7	97.562	0.608	1.115
GCM-15	59.630	0.742	3.832
GCM-22	87.973	0.704	3.836
GCM-15-NAA	44.648	0.279	3.839
GCM-15-DI	97.446	0.626	3.838

[a] BET specific surface.
[b] Total pore volume measured at P/P$_0$ = 0.99.
[c] The pore diameter is computed from the desorption branch of the isotherm using the BJH method.

Fig. 4. Nitrogen adsorption-desorption isotherm and the corresponding curves of the pore diameter distributions of GCM-7.

existence in g-C$_3$N$_4$, respectively [44–47], and the peak at 284.8 eV is ascribed to C=O of CH$_3$COOH. The N 1s spectrum in Fig. 5d shows three binding energy peaks at 398.2, 398.9 and 401.1 eV, which are associated with sp^2-hybridized in triazine rings (C−N=C) and amino functions carrying hydrogen (C−N−H) [48,49]. As shown in Fig. 5e, the Mo 3d spectrum reveals that the peaks at 228.6 eV and 232.1 eV are assigned to Mo 3d$_{5/2}$ and 3d$_{3/2}$, corroborating the presence of Mo IV oxidation states in MoS$_2$ [50]. It is noteworthy that a weak S 2s band appears at 224.9 eV, which is indicating the presence of S^{2-}. In order to further prove the valence of sulfur, Fig. 5f shows three peaks centered at 160.6, 161.7 and 162.8 eV. The peaks at 160.6 eV and 162.8 eV are corresponding to S 2p$_{3/2}$ and S 2p$_{1/2}$ of the sulfur element in MoS$_2$, respectively. In summary, the synthesized MoS$_2$ nanosheets are well integrated with GO/g-C$_3$N$_4$ in the mixture.

Fig. 6a displays the UV–vis diffuse reflectance (DRS) of the pure MoS$_2$ and a series of GCM samples. As shown, all studied samples show strong visible light absorption in the range of 400–800 nm. It can be seen that the optical absorption intensity of GCM nanocomposites is similar to that of pure MoS$_2$ (Fig. S5a), indicating that MoS$_2$ plays a
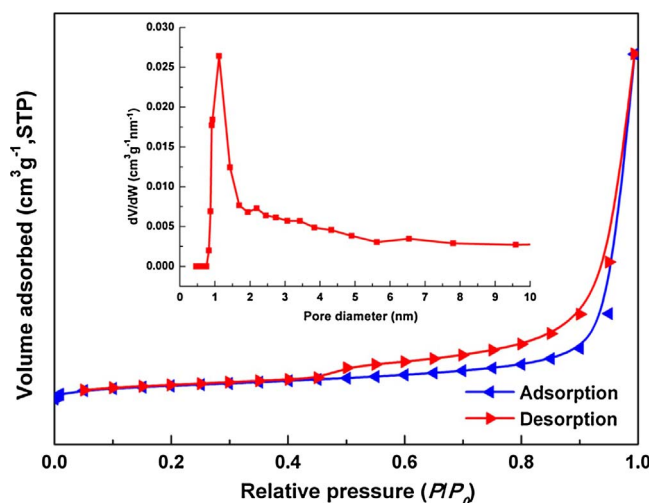
major role in composites. It is also implied that the higher visible light absorption of heterojunction between g-C$_3$N$_4$ and MoS$_2$ results in more photogenerated electron-hole pairs, which can better improve photo-catalytic performance. Besides, PL spectra of pure MoS$_2$ and as-prepared GCM samples can be observed from Fig. 6b. It can be found that the order of the photoluminescence intensity of these composites is: GCM-22 > GCM-15 > GCM-7 > GCM-15-NAA > GCM-0 > GCM-15-DI > pure MoS$_2$, confirming that the GCM-7 sample has a relatively long lifetime with photo-generated electron carrier. Moreover, with the decrease in the amount of CTAB, the photoluminescence intensity is significantly improved. Compared GCM-15 with GCM-15-DI, the effect of solvent on photoluminescence intensity is also significant.
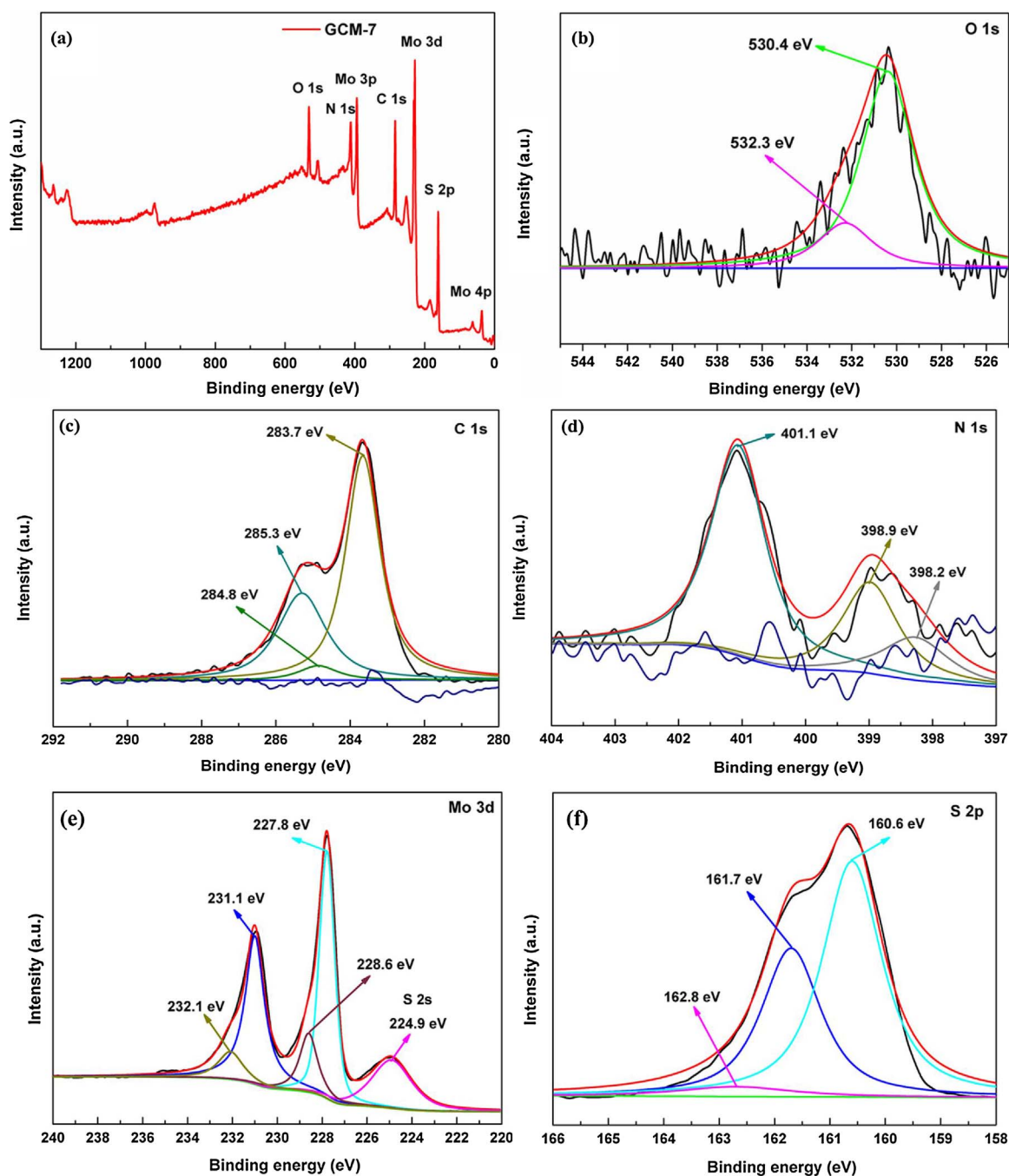
Fig. 5. XPS spectra of GCM-7: (a) survey, (b) O 1s, (c) C 1s, (d) N 1s, (e) Mo 3d, and (f) S 2p.

Meanwhile, PL intensity is affected by the acetic acid. Based on the above analysis, the results suggest that the interaction of the solvent and the surfactant can improve the performance of the photocatalyst. In addition, the enhanced visible light absorption and rapid separation efficiency play an important role in the significant photocatalytic activity of the GCM-7 hybrids.

3.2. Visible light-driven catalytic performance

To evaluate the potential application of GCM samples in environmental remediation, MB, RhB and CV were used as alternative contaminants to the visible photocatalytic properties of the synthesized material. Fig. 7a–c depicts the photocatalytic degradation curves of visible light catalytic efficiency for MB, RhB and CV by different samples. In this experiment, GCM-0, 7, 15, 22 appear different

photocatalytic performances. Among them, when CTAB is 0.07g, the photocatalytic performance of the sample is the best. The kinetics curve of MB degradation follows the pseudo-first-order linear transformation $\ln(C/C_0) = -kt$ [51]. Upon visible light irradiation, the MB is completely degraded by GCM-7 photocatalyst, and the degradation rate constant is reckoned $0.0592\,min^{-1}$ (Fig. 7d). In order to further demonstrate the excellent photocatalytic performance of GCM-7, the photocatalytic performance of GCM-7, GO/MoS_2 and $g-C_3N_4/MoS_2$ were compared. In Fig. S6a, it can be observed that GCM-7 possesses the best photocatalytic performance. The degradation efficiency of those composites confirms to the order: GCM-7 > CN/MoS_2 > GO/MoS_2, suggesting that the photocatalytic activity can be improved by the ternary $GO/g-C_3N_4/MoS_2$ flower-like heterojunctions. Meanwhile, the pseudo-first order reaction kinetics (k) of GCM-7 is 3.44 times and 3.54 times higher than that of the GO/MoS_2 and CN/MoS_2, respectively
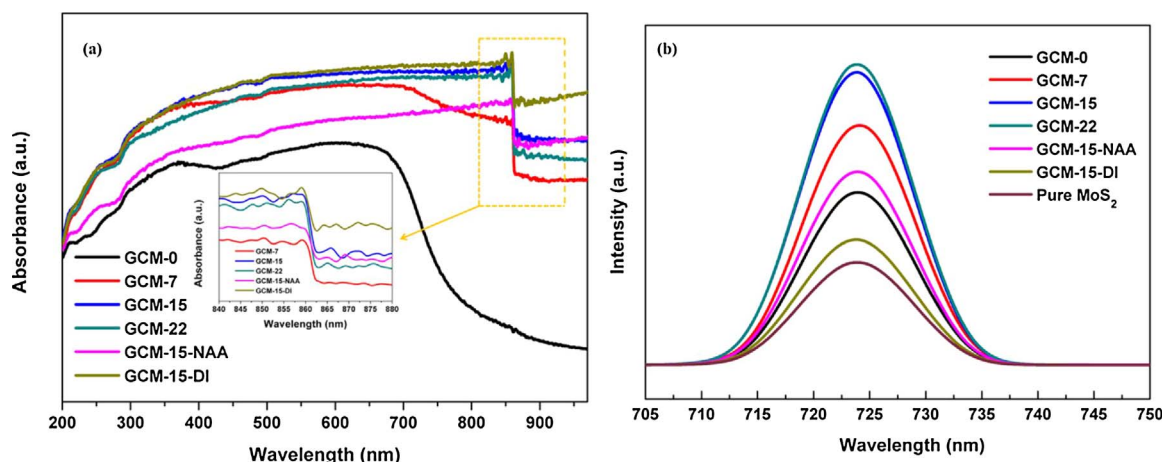
Fig. 6. UV–vis DRS spectra (a) and PL spectra (b) of different photocatalysts.

(Fig. S6b). Notably particularly, in the presence of the photocatalyst GCM-7 the removal efficiency of RhB and CV are achieved 77.2% and 70.3% under visible light exposure for 60 min. Under the same circumstances, the pseudo-first order reaction kinetics (k) of RhB and CV removal over the GCM-7 are $0.0155 \, min^{-1}$ and $0.0123 \, min^{-1}$, respectively (Fig. S7). The possible reason the amount of CTAB is different to cause a change in the number of photocatalytic active sites of MoS_2. Another reason is that the synergistic effects of $GO/g\text{-}C_3N_4$ promotes charge transfer and improve the separation efficiency of photoelectron-hole pairs.

For the GCM-15 and GCM-15-NAA samples, the effect of CH_3COOH

on the active site of MoS_2 is significant, which is similar to the report by other literatures [52,53]. Therefore, GCM-15-NAA photocatalyst has the lowest photodegradation efficiency for MB, RhB and CV under visible light irradiation. Parity GCM-15 and GCM-15-DI, the effect of the reaction solvent on the MoS_2 photocatalytic activity sites is obvious. In conclusion, the MoS_2 photocatalytic activity sites can be regulated by changes in external conditions.

In order to further explore the ability of the as-prepared samples to purify the environment, the removal ability of heavy metals Cr(VI) is used as an indicator of photocatalytic performance. It is observed that GCM-7 displays the better visible light-driven photocatalytic
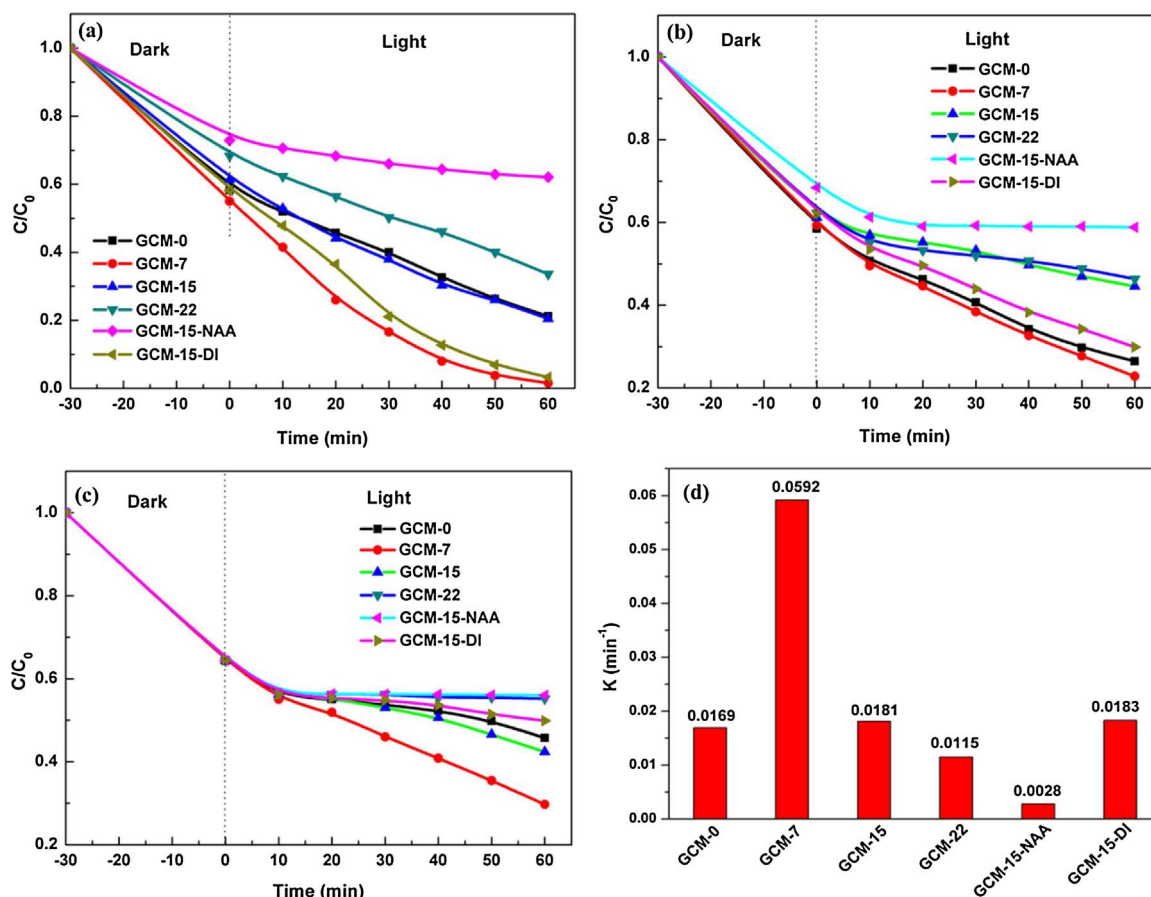

Fig. 7. Photodegradation of (a) MB, (b) RhB and (c) CV by using different samples under visible-light irradiation. (d) The apparent reaction rate constants (k) of MB using different photocatalysts after 60 min of visible light irradiation.
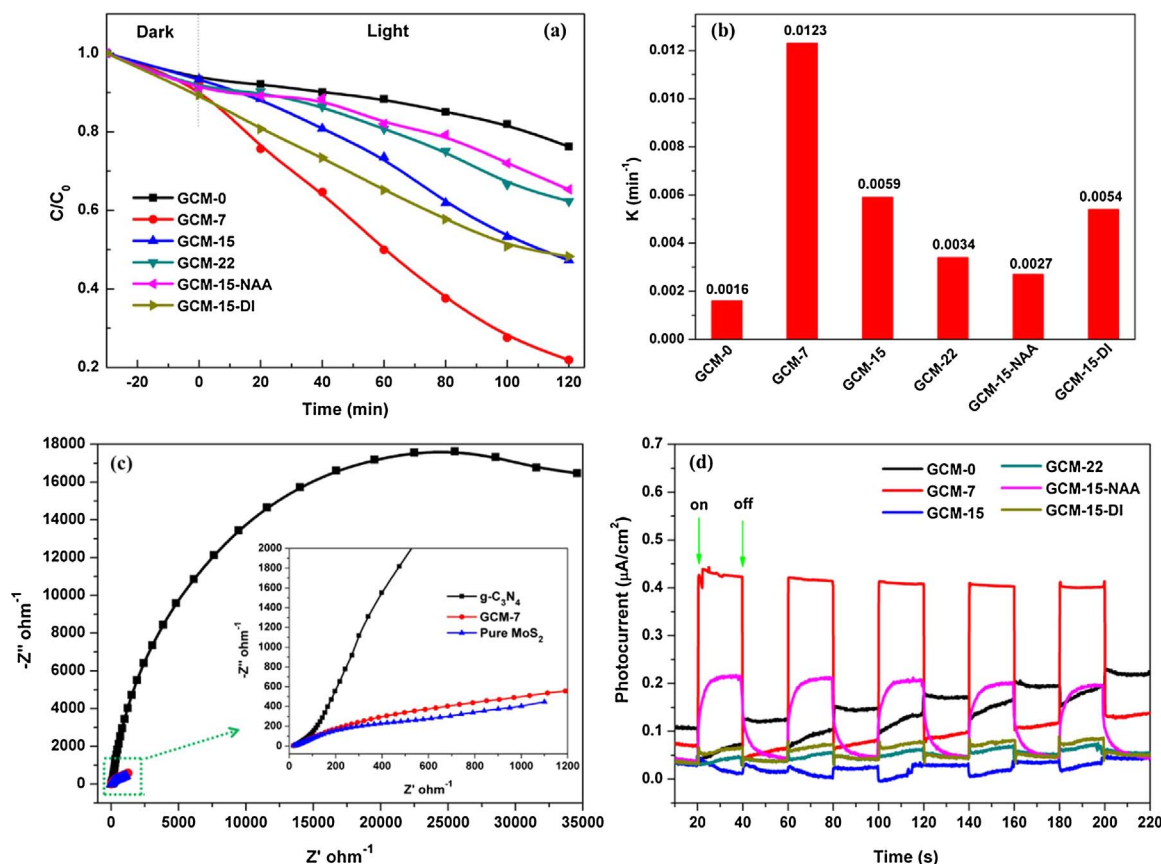
Fig. 8. Photocatalytic reduction curves (a) of the Cr (VI) and the pseudo-first-order degradation rate constants (k) of Cr (VI) (b) using different samples under visible-light illumination. Nyquist impedance plots (c) of g-C$_3$N$_4$,GCM-7 and pure MoS$_2$. (d) Transient photocurrent responses of different photocatalysts.

performance for Cr(VI) reduction, which is due to rapid electron transfer and improved light absorption (Fig. 8a). The reaction kinetics of Cr(VI) reduction is determined by plotting value of ln(C/C$_0$) versus illumination time, and the reaction rate constants (k) are calculated by pseudo-first order model ln(C/C$_0$) = −kt. The reduction rate constant of GCM-7 is computed as 0.0123 min^{-1}, which is 2.3 and 7.69 times higher than GCM-15-DI and GCM-0, respectively (Fig. 8b). Compared to other samples, GCM-7 shows the better reduction property, which suggests that enhanced electron transport efficiency plays an irreplaceable role in improving photocatalytic efficiency, because efficient electron transfer can reduce the recombination probability of electron-hole pairs. In addition, MoS$_2$ has more active sites, which provides more sites for photocatalysis.

To further illustrate the above conclusion, transfer performance and photo-induced charge separation were evaluated by EIS and photocurrent analysis. Fig. 8c displays the experimental Nyquist impedance plots of g-C$_3$N$_4$, GCM-7 and MoS$_2$. Compared with g-C$_3$N$_4$, the radius of Nyquist arc of GCM-7 is significantly smaller, which exhibits that MoS$_2$ and GO loading are propitious to enhance the charge transfer efficiency. The photocurrent-time curves for different photocatalysts are shown that in Fig. 8d. It can be observed that the photocurrent response of GCM-7 under visible light irradiation is significantly increased relative to other photocatalysts. It confirms that GCM-7 possesses a more efficient separation and migration of photo-induced charge carriers. The results can be implied to the fact that the flower-like heterojunctions are beneficial to electron transfer and suppression of direct recombination of photo-generated electrons and holes.

3.3. Reusability and stability of GO/g-C$_3$N$_4$/MoS$_2$ nanocomposites

In order to evaluate the practical application value of the catalyst,

the reusability and stability of GCM-7 were also studied. As seen in Fig. 9a, the cyclic stability of the composites was tested by 3 degradation cycle runs, and the photocatalytic activity of GCM-7 did not decrease significantly. Moreover, the XRD diffraction patterns (Fig. 9b) of GCM-7 before and after the reaction showed that the crystal structure of GCM-7 remained balanced. Taking into account the above results, it can be demonstrated that the GCM-7 nanocomposite is stable during photocatalysis process.

3.4. Photocatalytic mechanisms

Although we achieved a fascinating water purification performance through the GCM-7 mixture, a free radical trapping experimentwas conducted to further investigate the photocatalytic mechanism. Hence, we used ρ-benzoquinone, isopropanol and EDTA-2Na as the active particle quenchers for ·O$_2$$^-$, ·OH and h$^+$, respectively [54]. Obviously, the degradation of MB is inhibited in the presence of EDTA-2Na; however, the ρ-benzoquinone and isopropanol play a negligible inhibitory effect on MB degradation (Fig. 9c). Unexpectedly, the MB is degraded only 41.5% when EDTA-2Na is added, whose photodegradation effect is very different from that before. All the phenomena depict MB degradation relies on h$^+$ greatly rather than ·O$_2$$^-$ and ·OH. Fig. 9d shows a typical Mott-Schottky plot of g-C$_3$N$_4$, pure MoS$_2$ and GCM-7 measured at a frequency of 1 KHz in dark, which indicates that GCM-7 is an n-typed semiconductor. The estimated flat band potential of GCM-7 is −1.29 V vs SCE at pH 7.0 (equivalent to −1.05 V vs NHE) [55]. Accordingly, the conduction band potential (E$_{CB}$) of the GCM-7 is determined to be about −1.15 V vs NHE [56]. Based on the band gap energy calculated by UV–vis DRS spectra, the calculated optical bandgap for GCM-7 is 1.51 eV (Fig. S8). According to the empirical formula of E$_g$ = E$_{VB}$ − E$_{CB}$, the valence band potentials (E$_{VB}$) of GCM-7 is
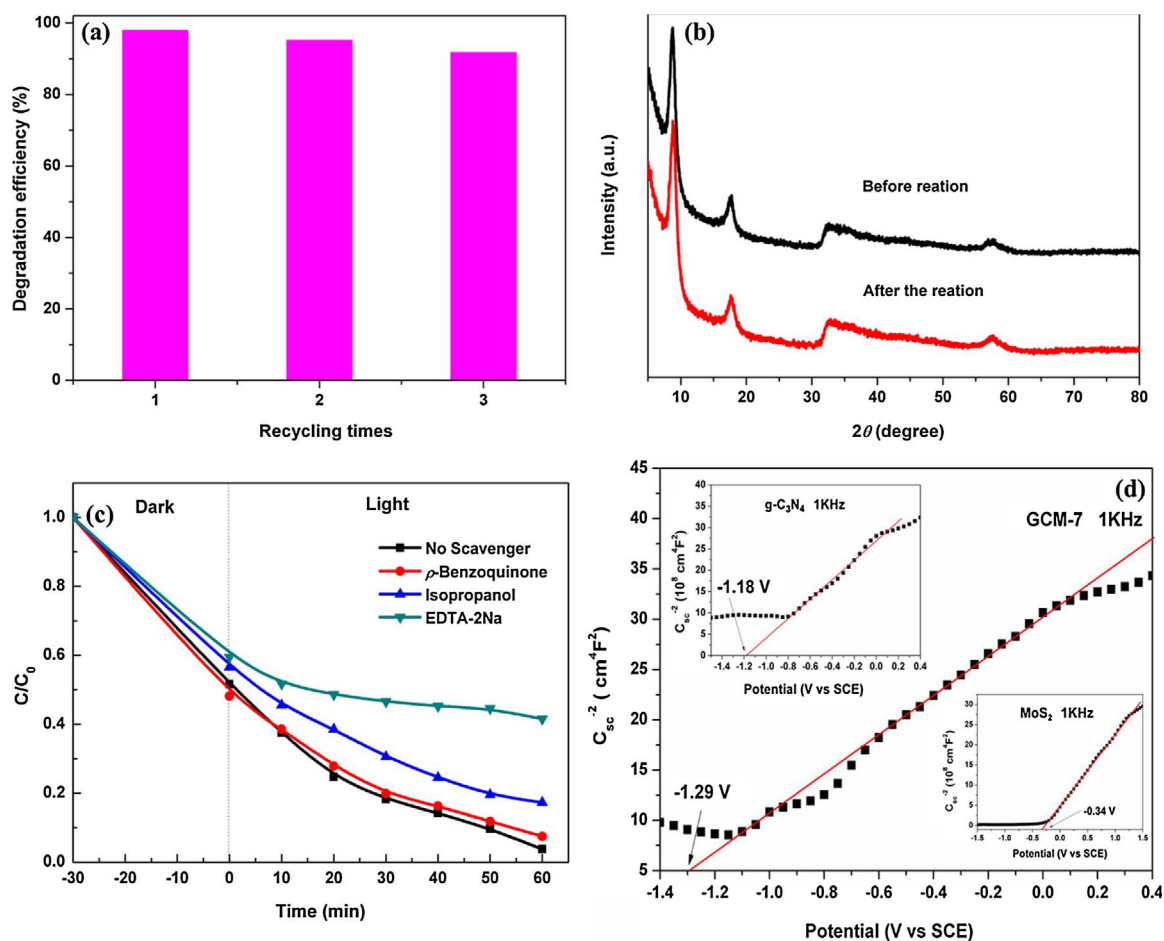
Fig. 9. (a) Recycled testing plots of the GCM-7 nanocomposite for MB, (b) XRD patterns of GCM-7 nanocomposite before and after the photocatalytic reaction and (c) Effects of different scavengers on the MB degradation with GCM-7. (d) Mott-Schottky plots of g-C$_3$N$_4$, pure MoS$_2$ and GCM-7.
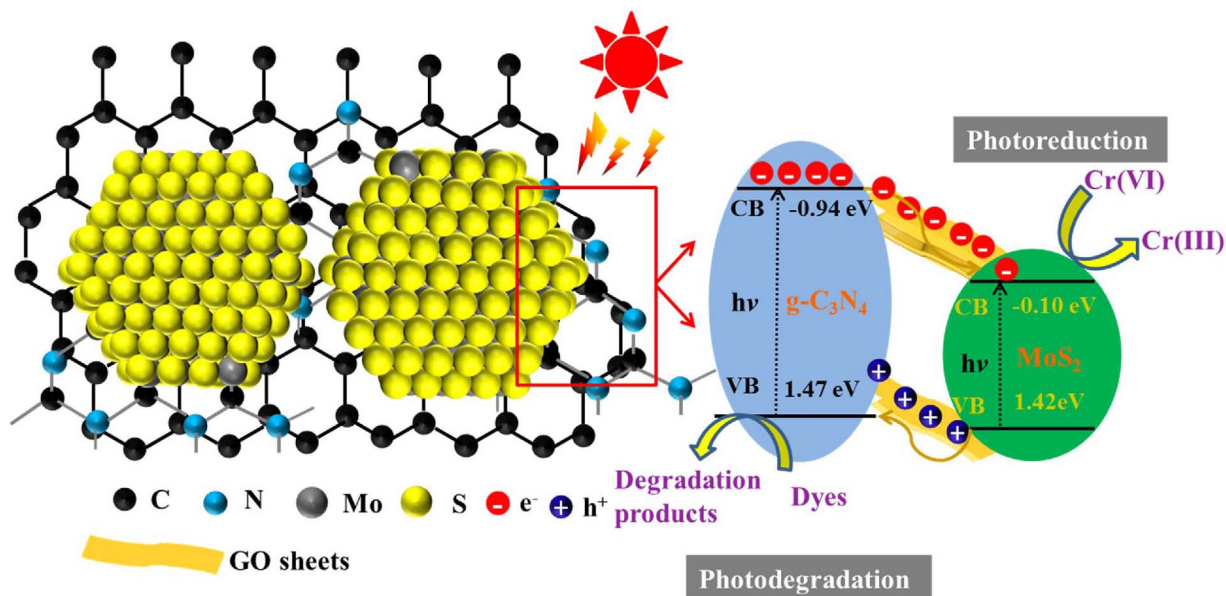

Fig. 10. Schematic drawing of the photocatalytic process and charge transfer mechanisms in the GO/g-C$_3$N$_4$/MoS$_2$ composites.

calculated to be 0.46 V vs NHE. Similarly, The band gap energy (E$_g$) of g-C$_3$N$_4$ and pure MoS$_2$ was estimated on the basis of the intercept of the tangents to the plots of (αhν)$^{1/2}$ (or (αhν)^2) vs. photo energy, as shown Figs. S5b and S9b. The band gaps of pure MoS$_2$ and g-C$_3$N$_4$ are 1.52 eV and 2.41 eV, individually. It is notable that the photo-induced electrons

are transported from the conduction band (CB) of g-C$_3$N$_4$ to the CB of MoS$_2$ so that Cr (VI) is reduced. Meanwhile, the holes from the valence band (VB) of MoS$_2$ can transfer to the VB of g-C$_3$N$_4$, which can reduce the compound charge and accumulate more free electrons in the CB of g-C$_3$N$_4$. Therefore, the internal electron regions are beneficial to charge

migration between g-C$_3$N$_4$ and MoS$_2$ with matching potential band potentials, resulting in improved photocatalytic performance of GCM-7. A well-combined GO/g-C$_3$N$_4$/MoS$_2$ heterojunction can promote the transfer of photogenerated electrons between g-C$_3$N$_4$ and MoS$_2$, while the function of GO provides a well-charged conductivity. In order to discuss the photocatalytic reaction, the photogenerated electron-hole charge transfer process is indicated in Fig. 10. Due to the shorter charge transfer path and good conductivity of GO, electron-hole recombination is greatly limited. Besides, MoS$_2$ is highly dispersed on the GO/g-C$_3$N$_4$ substrate, providing more photocatalytic active sites for the degradation of contaminants. Thus, it is foreseen that photocatalytic performance through GO/g-C$_3$N$_4$/MoS$_2$ photocatalysts can be significantly improved.

4. Conclusions

In summary, GO/g-C$_3$N$_4$/MoS$_2$ ternary nanocomposites have been rationally designed and synthesized via a simple one-pot solvothermal method. The dual effect of solvent and surfactant makes the photocatalytic effect of MoS$_2$ be improved significantly. Moreover, MoS$_2$ prepared by acidic conditions also contributes to the improvement of photocatalytic performance. Thus, the as-prepared photocatalysts exhibit superior photocatalytic performance toward degrading MB, RhB and CV. Furthermore, such hybrid nanojunctions also show photoreduction capacity of Cr (VI) under visible light irradiation. Excellent substrate material accelerates the transmission of photoelectrons and reduces the recombination of electron-hole pairs, all of which ensure improved photocatalytic activity. This work can be used to explore new ways to explore the application of MoS$_2$ materials for environmental purification applications.

Acknowledgements

Appendix A. Supplementary data

Supplementary material related to this article can be found, in the online version, at doi:https://doi.org/10.1016/j.apcatb.2018.01.063.

References

[1] K.M. Zhang, Z.G. Wen, Review and challenges of policies of environmental protection and sustainable development in China, J. Environ. Manage. 88 (2008) 1249–1261.
[2] R. Liang, F. Jing, L. Shen, N. Qin, L. Wu, MIL-53(Fe) as a highly efficient bifunctional photocatalyst for the simultaneous reduction of Cr(VI) and oxidation of dyes, J. Hazard. Mater. 287 (2015) 364–372.
[3] X. Bai, C. Sun, S. Wu, Y. Zhu, Enhancement of photocatalytic performance via a P3HT-g-C3N4 heterojunction, J. Mater. Chem. A 3 (2015) 2741–2747.
[4] B.Y. Guan, X.Y. Yu, H.B. Wu, X.W.D. Lou, Complex nanostructures from materials based on metal-organic frameworks for electrochemical energy storage and conversion, Adv. Mater. 29 (2017).
[5] D. Liu, Y. Lv, M. Zhang, Y. Liu, Y. Zhu, R. Zong, Y. Zhu, Defect-related photoluminescence and photocatalytic properties of porous ZnO nanosheets, J. Mater. Chem. A 2 (2014) 15377.
[6] X. Zhang, H. Li, F. Hou, Y. Yang, H. Dong, N. Liu, Y. Wang, L. Cui, Synthesis of highly efficient Mn2O3 catalysts for CO oxidation derived from Mn-MIL-100, Appl. Surf. Sci. 411 (2017) 27–33.
[7] S. Wang, B.Y. Guan, L. Yu, X.W.D. Lou, Rational design of three-layered TiO2 @Carbon@MoS2 hierarchical nanotubes for enhanced lithium storage, Adv. Mater. 29 (2017).
[8] W. Jiang, W. Luo, R. Zong, W. Yao, Z. Li, Y. Zhu, Polyaniline/carbon nitride nanosheets composite hydrogel: a separation-free and high-efficient photocatalyst with 3D hierarchical structure, Small 12 (2016) 4370–4378.
[9] S. Wang, B.Y. Guan, Y. Lu, X.W.D. Lou, Formation of hierarchical In2S3-CdIn2S4 heterostructured nanotubes for efficient and stable visible light CO2 reduction, J. Am. Chem. Soc. 139 (2017) 17305–17308.
[10] M. Cabán-Acevedo, M.L. Stone, J.R. Schmidt, J.G. Thomas, Q. Ding, H.-C. Chang, S. Jin, Ecient hydrogen evolution catalysis usingternary pyrite-type cobalt phosphosulphide, Nat. Mater. 14 (2015) 1245–1251.
[11] M. Chhowalla, H.S. Shin, G. Eda, L.J. Li, K.P. Loh, H. Zhang, The chemistry of two-dimensional layered transition metal dichalcogenide nanosheets, Nat. Chem. 5 (2013) 263–275.
[12] K.F. Mak, C. Lee, J. Hone, J. Shan, T.F. Heinz, Atomically thin MoS2: a new direct-gap semiconductor, Phys. Rev. Lett. 105 (2010) 136805.
[13] L.A. King, W. Zhao, M. Chhowalla, D.J. Riley, G. Eda, Photoelectrochemical properties of chemically exfoliated MoS2, J. Mater. Chem. A 1 (2013) 8935.
[14] S.Z. Butler, S.M. Hollen, L. Cao, J.E. Goldberger, Progress, challenges, and opportunities in two-dimensional materials beyond graphene, ACS Nano 7 (2013) 2898–2926.
[15] Y. Hou, A.B. Laursen, J. Zhang, G. Zhang, Y. Zhu, X. Wang, S. Dahl, I. Chorkendorff, Layered nanojunctions for hydrogen-evolution catalysis, Angew. Chem. Int. Ed. Engl. 52 (2013) 3621–3625.
[16] Y. Gao, C. Chen, X. Tan, H. Xu, K. Zhu, Polyaniline-modified 3D-flower-like molybdenum disulfide composite for efficient adsorption/photocatalytic reduction of Cr(VI), J. Colloid Interface Sci. 476 (2016) 62–70.
[17] C. Zhu, L. Zhang, B. Jiang, J. Zheng, P. Hu, S. Li, M. Wu, W. Wu, Fabrication of Z-scheme Ag3PO4/MoS2 composites with enhanced photocatalytic activity and stability for organic pollutant degradation, Appl. Surf. Sci. 377 (2016) 99–108.
[18] D. Lu, H. Wang, X. Zhao, K.K. Kondamareddy, J. Ding, C. Li, P. Fang, Highly efficient visible-light-induced photoactivity of Z-scheme g-c3n4/Ag/MoS2 ternary photocatalysts for organic pollutant degradation and production of hydrogen, ACS Sustain. Chem. Eng. 5 (2017) 1436–1445.
[19] Y. Jiang, D. Wang, J. Li, M. Li, Z. Pan, H. Ma, G. Lv, W. Qu, L. Wang, Z. Tian, Designing MoS2 nanocatalysts with increased exposure of active edge sites for anthracene hydrogenation reaction, Catal. Sci. Technol. 7 (2017) 2998–3007.
[20] Z. Wang, T. Chen, W. Chen, K. Chang, L. Ma, G. Huang, D. Chen, J.Y. Lee, CTAB-assisted synthesis of single-layer MoS2-graphene composites as anode materials of Li-ion batteries, J. Mater. Chem. A 1 (2013) 2202–2210.
[21] I. Bezverkhy, P. Afanasiev, M. Lacroix, Aqueous preparation of highly dispersed molybdenum sulfide, Inorg. Chem. 39 (2000) 5416–5417.
[22] X. Zeng, W. Qin, Synthesis of MoS2 nanoparticles using MoO3 nanobelts as precursor via a PVP-assisted hydrothermal method, Mater. Lett. 182 (2016) 347–350.
[23] Y. Guo, L. Gan, C. Shang, E. Wang, J. Wang, A cake-style CoS2@MoS2/RGO hybrid catalyst for efficient hydrogen evolution, Adv. Funct. Mater. 27 (2017) 1602699.
[24] H. Wang, J.T. Robinson, G. Diankov, H. Dai, Nanocrystal growth on graphene with various degrees of oxidation, J. Am. Chem. Soc. 132 (2010) 3270–3271.
[25] H. Yang, K. Lv, J. Zhu, Q. Li, D. Tang, W. Ho, M. Li, S.A.C. Carabineiro, Effect of mesoporous g-C3N4 substrate on catalytic oxidation of CO over Co3O4, Appl. Surf. Sci. 401 (2017) 333–340.
[26] Y. Ding, Y. Zhou, W. Nie, P. Chen, MoS2-GO nanocomposites synthesized via a hydrothermal hydrogel method for solar light photocatalytic degradation of methylene blue, Appl. Surf. Sci. 357 (2015) 1606–1612.
[27] J. Li, E. Liu, Y. Ma, X. Hu, J. Wan, L. Sun, J. Fan, Synthesis of MoS2/g-C3N4 nanosheets as 2D heterojunction photocatalysts with enhanced visible light activity, Appl. Surf. Sci. 364 (2016) 694–702.
[28] Q. Xu, C. Jiang, B. Cheng, J. Yu, Enhanced visible-light photocatalytic H2-generation activity of carbon/g-C3N4 nanocomposites prepared by two-step thermal treatment, Dalton Trans. 46 (2017) 10611–10619.
[29] Z. Tong, D. Yang, J. Shi, Y. Nan, Y. Sun, Z. Jiang, Three-dimensional porous aerogel constructed by g-C3N4 and graphene oxide nanosheets with excellent visible-light photocatalytic performance, ACS Appl. Mater. Interfaces 7 (2015) 25693–25701.
[30] W. Wan, S. Yu, F. Dong, Q. Zhang, Y. Zhou, Efficient C3N4/graphene oxide macroscopic aerogel visible-light photocatalyst, J. Mater. Chem. A 4 (2016) 7823–7829.
[31] D.C. Marcano, D.V. Kosynkin, J.M. Berlin, J.M. Tour, Improved synthesis of graphene oxide, ACS Nano 4 (2010) 4806–4814.
[32] K. Zhao, X. Zhang, L. Zhang, The first BiOI-based solar cells, Electrochem. Commun. 11 (2009) 612–615.
[33] C. Liu, L. Wang, Y. Tang, S. Luo, Y. Liu, S. Zhang, Y. Zeng, Y. Xu, Vertical single or few-layer MoS2 nanosheets rooting into TiO2 nanofibers for highly efficient photocatalytic hydrogen evolution, Appl. Catal. B: Environ. 164 (2015) 1–9.
[34] W. Dai, J. Yu, Y. Deng, X. Hu, T. Wang, X. Luo, Facile synthesis of MoS2/Bi2WO6 nanocomposites for enhanced CO2 photoreduction activity under visible light irradiation, Appl. Surf. Sci. 403 (2017) 230–239.
[35] R. Tang, R. Yin, S. Zhou, T. Ge, Z. Yuan, L. Zhang, L. Yin, Layered MoS2 coupled MOFs-derived dual-phase TiO2 for enhanced photoelectrochemical performance, J. Mater. Chem. A 5 (2017) 4962–4971.
[36] D. Wang, Y. Xiao, X. Luo, Z. Wu, Y.-J. Wang, B. Fang, Swollen ammoniated MoS2 with 1T/2H hybrid phases for high-rate electrochemical energy storage, ACS Sustain. Chem. Eng. 5 (2017) 2509–2515.
[37] D. Wang, X. Zhang, Y. Shen, Z. Wu, Ni-doped MoS2 nanoparticles as highly active hydrogen evolution electrocatalysts, RSC Adv. 6 (2016) 16656–16661.
[38] S. Yang, Y. Gong, J. Zhang, L. Zhan, L. Ma, Z. Fang, R. Vajtai, X. Wang, P.M. Ajayan, Exfoliated graphitic carbon nitride nanosheets as efficient catalysts for hydrogen evolution under visible light, Adv. Mater. 25 (2013) 2452–2456.
[39] H. Song, B. Wang, Q. Zhou, J. Xiao, X. Jia, Preparation and tribological properties of MoS2/graphene oxide composites, Appl. Surf. Sci. 419 (2017) 24–34.
[40] S. Han, K. Liu, L. Hu, F. Teng, P. Yu, Y. Zhu, Superior adsorption and regenerable dye adsorbent based on flower-like molybdenum disulfide nanostructure, Sci. Rep. 7 (2017) 43599.
[41] X. Dai, M. Xie, S. Meng, X. Fu, S. Chen, Coupled systems for selective oxidation of aromatic alcohols to aldehydes and reduction of nitrobenzene into aniline using CdS/g-C3N4 photocatalyst under visible light irradiation, Appl. Catal. B: Environ. 158–159 (2014) 382–390.

[42] L. Shen, S. Liang, W. Wu, R. Liang, L. Wu, CdS-decorated UiO-66(NH2) nano-composites fabricated by a facile photodeposition process: an efficient and stable visible-light-driven photocatalyst for selective oxidation of alcohols, J. Mater. Chem. A 1 (2013) 11473.

[43] X. Hao, Z. Jin, H. Yang, G. Lu, Y. Bi, Peculiar synergetic effect of MoS2 quantum dots and graphene on metal-organic frameworks for photocatalytic hydrogen evolution, Appl. Catal. B: Environ. 210 (2017) 45–56.

[44] L. Liu, J. Wang, C. Wang, G. Wang, Facile synthesis of graphitic carbon nitride/ nanostructured α-Fe2O3 composites and their excellent electrochemical performance for supercapacitor and enzyme-free glucose detection applications, Appl. Surf. Sci. 390 (2016) 303–310.

[45] H. Wang, X. Yuan, Y. Wu, G. Zeng, X. Chen, L. Leng, H. Li, Synthesis and applications of novel graphitic carbon nitride/metal-organic frameworks mesoporous photocatalyst for dyes removal, Appl. Catal. B: Environ. 174–175 (2015) 445–454.

[46] B. Zhu, P. Xia, Y. Li, W. Ho, J. Yu, Fabrication and photocatalytic activity enhanced mechanism of direct Z-scheme g-C3N4/Ag2WO4 photocatalyst, Appl. Surf. Sci. 391 (2017) 175–183.

[47] H. Liu, T. Kuila, N.H. Kim, B.-C. Ku, J.H. Lee, In situ synthesis of the reduced graphene oxide–polyethyleneimine composite and its gas barrier properties, J. Mater. Chem. A 1 (2013) 3739.

[48] J. Lv, K. Dai, J. Zhang, L. Geng, C. Liang, Q. Liu, G. Zhu, C. Chen, Facile synthesis of Z-scheme graphitic-C3N4/Bi2MoO6 nanocomposite for enhanced visible photo-catalytic properties, Appl. Surf. Sci. 358 (2015) 377–384.

[49] X. Lu, Y. Jin, X. Zhang, G. Xu, D. Wang, J. Lv, Z. Zheng, Y. Wu, Controllable synthesis of graphitic C3N4/ultrathin MoS2 nanosheet hybrid nanostructures with enhanced photocatalytic performance, Dalton Trans. 45 (2016) 15406–15414.

[50] H. Li, F. Xie, W. Li, B.D. Fahlman, M. Chen, W. Li, Preparation and adsorption capacity of porous MoS2 nanosheets, RSC Adv. 6 (2016) 105222–105230.

[51] N. Liu, W. Huang, X. Zhang, L. Tang, L. Wang, Y. Wang, M. Wu, Ultrathin graphene oxide encapsulated in uniform MIL-88A(Fe) for enhanced visible light-driven photodegradation of RhB, Appl. Catal. B: Environ. 221 (2018) 119–128.

[52] T. Yang, X. Feng, Q. Tang, W. Yang, J. Fang, G. Wang, W. Shi, L. Shi, P. Ding, A facile method to prepare MoS2 with nanolameller-like morphology, J. Alloys Compd. 509 (2011) L236–L238.

[53] W.-J. Li, E.-W. Shi, J.-M. Ko, Z.-z. Chen, H. Ogino, T. Fukuda, Hydrothermal synthesis of MoS2 nanowires, J. Cryst. Growth 250 (2003) 418–422.

[54] S. Chen, Y. Hu, S. Meng, X. Fu, Study on the separation mechanisms of photo-generated electrons and holes for composite photocatalysts g-C3N4-WO3, Appl. Catal. B: Environ. 150–151 (2014) 564–573.

[55] C. Zhang, L. Ai, J. Jiang, Graphene hybridized photoactive iron terephthalate with enhanced photocatalytic activity for the degradation of rhodamine B under visible light, Ind. Eng. Chem. Res. 54 (2014) 153–163.

[56] W. Huang, N. Liu, X. Zhang, M. Wu, L. Tang, Metal organic framework g-C3N4/ MIL-53(Fe) heterojunctions with enhanced photocatalytic activity for Cr(VI) reduction under visible light, Appl. Surf. Sci. 425 (2017) 107–116.